Soft Matter

Accepted Manuscript

ROYAL SOCIETY OF CHEMISTRY

www.rsc.org/softmatter

ARTICLE Journal Name

A Bead-Spring Model for Running and Tumbling of Flagellated Swimmers: Detailed Predictions Compared to Experimental Data for E. coli

Cite this: DOI: 10.1039/x0xx00000x

Miqiu Kong[a], Yan Wu[c,d], Guangxian Li[a,b], and Ronald G. Larson[c*]

Received ooth January 2012,
Accepted ooth January 2012

DOI: 10.1039/x0xx00000x

www.rsc.org/

To study the swimming of the multi-flagellated bacterium *Escherichia coli*, we deploy a bead-spring hydrodynamic model (Watari and Larson 2010), whose body and flagellar geometry, motor torques, and motor reversals are adjusted to match the experimental observations of the Berg group (Turner et al. 2000; Darnton et al. 2007) during both running and tumbling of the bacterium. In this model, hydrodynamic interactions, which drive swimming, flagellar bundling, and unbundling during swimming and tumbling, are imposed by treating the beads as Stokeslets, imposing torques and counter-torques on the body and flagellum at the flexible joint connecting them to represent the action of motor, and using the Rotne-Prager tensor to model their hydrodynamic interactions with other beads. We explore the behavior of coarse-grained (60-bead) and refined (120-bead) versions of the model, and show that predictions of running speed, helical and body rotation rates, body wobble rates and angles, average tumbling angles, range of tumbling angles, and flagellar re-bundling times are in good agreement with experimental observations by Berg and coworkers. We find that variation in tumbling angle arises from variation in flagellar number and location on the bacterial body, variations in polymorphic transitions of the filaments, and especially from variations in the duration of the tumbling time, which is roughly linearly correlated with tumbling time up to tumbling angles of around 40-50° and more weakly thereafter. The accuracy of the model suggests its usefulness for future studies of swimming of other flagellated swimmers, for predictions of collective phenomena, and for tuning parameters of coarser-grained swimmer models to achieve greater realism.

1. Introduction

The individual and collective dynamics of bacterial micro-swimmers, such as *E. coli*, have been studied extensively to improve understanding of *E. coli* and self-propelled micro-swimmers generally, and for applications in medicine or nano-technology. [1-9] Multi-flagellated bacteria such as *E. coli* consist of a body with prolate spheroidal shape (with short and long axes of lengths approximately 1 and 2 μm, respectively, for *E. coli*), with multiple flagella (typically 2 to 5 for *E. coli*) with flagellar length of around 7.3± 2.4 μm, based on observations of flagella dyed with stains that produced longest length. [10] The flagellum has a helical shape and is linked to the body by a flexible hook, which is driven at its base by a rotary motor. Bacteria that swim by rotating flagellar filaments have two modes of swimming, namely straight swimming called a "run" and directionally random swimming, called a "tumble". [11, 12] The flagella apparently grow at random locations on the surface of the cell, and during a run they all rotate in the same direction and bundle into a single helical propeller, while during a tumble, one or more flagella counter-rotate and depart the bundle; the disordered flow thereby created causes the tumbling motion, which the bacterium uses to reorient its swimming direction in hopes of finding nutrients. *E. coli* helical flagella are observed to have four distinct shapes, namely normal, semi-coiled, curly 1, and curly 2. The normal shape occurs during a run. When the motor driving at least one of the flagella counter-rotates (causing a tumble), the counter-rotating flagellum changes from normal to the semi-coiled and then to the curly 1 state. While the normal filament is a left-handed helix with pitch of ~2.5 μm and helix diameter of ~0.5 μm, the semi-coiled state is a right-handed helix with half the normal pitch but retaining the normal diameter; the curly 1 state is a right-handed helix with half the normal pitch and half the normal diameter. [10, 12] (The curly 2 state is also a right handed helix, but does not occur in normal swimming; it can be induced by pinning the filament to a glass surface. [10]) After the bacterium tumbles for a duration of around 0.14±0.08 s, [10] the reversely rotating motor changes its rotation back to its normal direction; the flagellum transforms back to the normal state and re-joins the bundle, leading to a new run.

Various theoretical approaches have been used to model the swimming and the collective behaviour of flagellated bacteria, such as the dipole model, [13] the two-bead swimmer model, [14-16] the three-bead swimmer model, [17, 18] and multiple flagella anchored at a fixed position. [19, 20] More detailed models have generally focused on the hydrodynamics of flagella without the bacterial body and without polymorphic transitions; results have been published for both a single flagellum, [21-24] and a set of three flagella, in both cases without a body. [25] None of these models are complete enough to simulate both running and tumbling of a whole bacterium. Motivated by simulations of

polymer molecules, Watari and Larson [26] developed a rather simple bead-spring "whole-swimmer" model of an *E. coli* swimmer that captures much of the hydrodynamics of swimming, including the runs and tumbles, as well as the observed tendency of the bacterium to swim towards flat surfaces and swim there in a clockwise direction (when viewed with the swimmer in the foreground and surface in the background). [26] Hydrodynamic interactions that create swimming as well as flagellar bundling and unbundling during swimming and tumbling are imposed by treating the beads as Stokeslets, using the Rotne-Prager tensor.

The objective of this paper is to use both coarse-grained and refined versions of this whole-swimmer model to predict running speed, helical and body rotation rates, motor rotation rate, body wobble angles, and tumbling dynamics, and to compare the results with experimental observations by Berg and coworkers. We analyze how the "tumbling angle," which is the angle through which the bacterium's swimming direction rotates in a tumble, is affected by the number and arrangements of the flagella on the bacterium, by shape transitions, and by tumbling time. We show that the refined version of the model is successful in predicting the experimental observations in running and tumbling if the body diameter is chosen to be 1 μm, and the time constant of the model, or equivalently the motor torque, is chosen to give the experimentally observed flagellar bundle rotation rate. (The fitted motor torque is within a factor of two of the best experimental estimates of its value.) This validated model could, in the future, be used to tune the parameters of much simpler models, which would allow realistic simulation of the collective phenomena of many such swimmers to be predicted.

2. Simulation methods

In the model of Watari and Larson, [26] the *E. coli* body and flagella are built out of beads and stiff Fraenkel springs with bending and torsional potentials to hold the body shape (radius and length) and flagella shape (helical pitch, radius, and length) close to their experimental values in the presence of hydrodynamic stresses. We here review that model briefly, but leave out the equations, which can be found in Ref. [26]. The model contains a spring potential ϕ_s that controls the distance between two adjacent connected beads, a bending potential ϕ_b that controls the bending angle formed by three connected beads, and a torsional potential ϕ_t that controls the torsional angle formed by four connected beads in the helical flagellum. Additionally, we employ a spring-spring interaction potential ϕ_{ss} to prevent two springs from crossing each other. [27]

The "coarse-grained" geometry, which contains a total of 60 beads, with 15 beads in the cell body and 15 beads in each of three flagella attached to the body, was depicted in Ref. [26]. The quantitative accuracy is here improved by increasing the number of beads to 120, with 30 beads in the body and 30 beads in each of the (typically three) flagella attached to the body; the refined geometry is shown in Figure 1. Note that the shape of the body and of each flagellum are kept nearly rigid with the employed potentials. [26] In the refined model, the body cross section is a pentagon, while in the coarse-grained model, a triangular cross section is used. These body shapes determine the positions at which flagella can be attached, since each must be attached to a body bead, and cannot be attached to beads on the ends of the body, because imposition of torques requires the presence of not only a bead at the attachment site of the flagellum, but also beads both fore and aft of the attachment site. As discussed later, to explore more thoroughly the role of flagellar location on bacterial tumbling, we also consider swimmers with nine layers of beads in the body, as opposed to the five depicted in Figure 1.

The different helical shapes of the flagella (normal, semi-coiled, and curly 1) are imposed by the choice of bending and torsional potentials for the springs in the flagella, which are switched from those for a normal shape to those for a semi-coiled or a curly 1 shape to initiate tumbling. (The switch in potential is usually done sequentially, starting from the attachment point to the body, and progressing rapidly (within about 0.01 s) to the end of the flagellum, mimicking the behavior observed experimentally for *E. coli*, for which the transformation takes around 0.01 s. [10]) The action of the motor is mimicked by imposing a torque on each flagellum and a counter-torque on the body to persevere overall torque balance. The hook that connects the body to a flagellum is modeled with three beads, one of them a body bead and the other two the first two flagellum beads. [26] Because of its flexibility, no bending potential is applied to the hook as long as the bending angle formed by these three beads exceeds 90°. [28] A bending potential is applied for smaller angles to keep the flagellum from intersecting the body. We apply torques on each flagellum and the body to represent the action of a motor. [26]

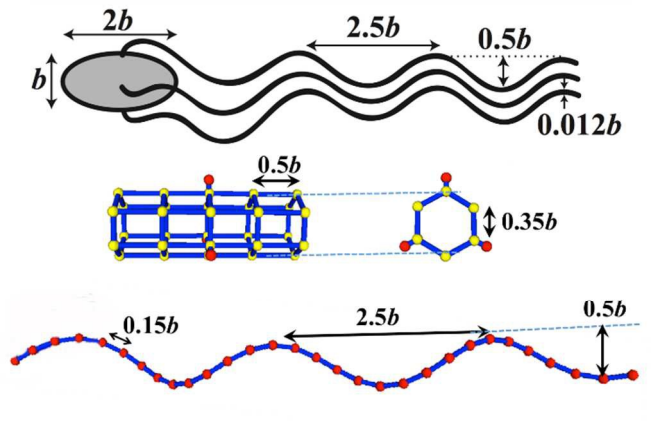

Figure 1 The bead-spring model of typical *E. coli* cell with flagella in the normal state. Here b is the half the length of the long axis of the body, and is taken as the unit of length in our simulations, and has the value 1 μm for *E. coli*. The red circles in the body represent the positions of first bead of each flagellum attached by a hook in one particular arrangement of flagella.

The motion of each bead of a modeled cell at low Reynolds number is treated as a Stokeslet that generates a flow field that affects all beads through a Rotne-Prager tensor,

$$\boldsymbol{r}_i(t+\Delta t) = \boldsymbol{r}_i(t) + \left\{\sum_{j=1}^{N} \boldsymbol{H}_{ij} \cdot \boldsymbol{f}_j\right\}\Delta t,$$

where $\boldsymbol{r}_i(\boldsymbol{t})$ is the position vector of bead i at time t; $\boldsymbol{f}_j$ is the summation of forces originating from the torques and potential forces on bead j; N is the total number of beads in a model cell; $\boldsymbol{H}_{ij}$ is the Rotne-Prager-Yamakawa hydrodynamic interaction tensor; [29-31] and Δt is the time increment in the simulation. Note that we ignore the effect of the Brownian motion here, which generates motions that are significantly weaker than those driven by the motors. For a run, all torques are applied in such a way that all flagella rotate counterclockwise when viewed from behind the cell. For a tumble, the torque on one flagellum is reversed so that the flagellum rotates in the opposite direction from the others. At the beginning of a tumble, the equilibrium bending and torsional angles of the flagellum attached to the motor are switched to the angles for the semi-coiled state and at the halfway point of a tumble to the angles of curly 1 state to mimic the polymorphic transformations. Table 1 gives the parameters of the model for both the coarse-grained (60-bead) and refined (120-bead) swimmers; the precise definitions of the parameters and the equations in which they appear are given in ref. 20.

Table 1. Simulation parameters

Parameter type	Symbol	Meaning	Value	
			60 beads	120 beads
Common	a	Radius of bead.	$0.1b$	$0.06b$
	H	Spring constant.	$10T/b$	$1000T/b$
	s	Spring stretch parameter.	0.1	0.1
	k_b	Bending potential constant.	$20T$	$30T$
	k_t	Torsional potential constant.	$10T$	$5T$
	-	Number of flagella on a cell.	1-3	1-6
	Δt	Time increment in simulations.	$10^{-3}\tau$	$10^{-5}\tau$
Body	-	Number of beads.	15	30
	L	Equilibrium spring length.	variable	variable
Flagellum	-	Number of beads.	15	30
	L	Equilibrium spring length.	$0.58\,b$	$0.29\,b$
	θ_0^{bend}	Equilibrium bending angle.	$142°/90°/105°^{\dagger}$	$161°/138°/142°^{\dagger}$
	$\theta_0^{torsion}$	Equilibrium torsional angle.	$-60°/65°/120°^{\dagger}$	$-30°/32.5°/60°^{\dagger}$
	A_{ss}	Spring-spring potential constant.	$1.0T$	$1.0T$
	α_{ss}	Characteristic range of spring-spring potential.	$0.2\,b$	$0.2\,b$
	_	Cut-off length of spring-spring potential.	$0.2\,b$	$0.2\,b$

The symbols b and T are half the length of the long axis of the body and the magnitude of the torque applied by a motor to each end of the hook.

*See Fig.1 in Ref. [26] and Fig.1 in this paper.

†Values for normal/semi-coiled/curly 1 conformation, respectively.

We choose three input parameters with physical units: b (half the length of the long axis of the body, which is around $b = 1\ \mu m$ for *E. coli*); η (solvent viscosity $\eta = 10^{-3}$ Pa · s); and T (magnitude of the torque given by a motor to each end of hook, $T \approx 1200$ pN · nm [12]). Therefore, we scale length, time and energy with b, $\tau = \eta b^3/T$ and T, respectively. All parameters used in simulations are shown in Table 1. To determine the efficiency of the rotation and tumbling behaviors of the model, the coarse-grained and refined versions of the model are used in what follows. The torque applied by each motor is somewhat uncertain, and some of the torque is wasted in frictional interactions between the bundled flagella. [12] Since our bead-spring model cannot capture the internal friction produced by lubrication forces exerted between tightly bundled flagella, [6] we do not expect our model to predict the correct relationship between motor torque and swimming speed. Instead, as described below, we will use the model's computed flagellar bundle rotation speed as a "clock" that sets a timescale that we will then use for making quantitative comparisons between model predictions and experimental observations. In particular, the tumbling time in the simulation will be set to be comparable to the experimental times, measured in units of flagellar bundle rotations. Although the duration of the run mode has no direct effect on the tumbling angle, the phase angle of the flagellar bundle at the start of the tumble may affect the resulting tumbling angle. Thus, runs of random intervals are included in the simulations prior to tumbles, so that the statistics of tumbling angles includes all possible flagellar phase angles at the start of tumbling. Also each tumbling motion was simulated multiple times to obtain averages and standard deviations of tumbling angles.

3. Results and discussion

3.1 Rotation rates and swimming speed for a cell during running

Rotation rates and swimming speeds during a run are given in Table 2. An example of the motions of a bead in the body (thick lines) and a bead in a flagellum (thin lines) are given in Figure 2a during running of a typical 60-bead coarse-grained model bacterium. The oscillatory patterns in the coordinate values

reflect the flagellar and body rotation rates, and these are extracted by fast Fourier transformation (FFT), which yields the rotation rates of the body and flagella of the cell during running. The FFT of any of the bead coordinates, for either flagellum or body, give the two peak frequencies shown in Fig. 2b, the higher of which gives the rotation speed of the flagellar bundle, while the lower of them is the body rotation rate. (Both body and flagellar beads show both peaks at the same positions, since the motions of body and flagella are coupled to each other.)

Using this method, the rotation rates of the body and flagellar bundle of different swimmers are determined, and the results are shown in Table 2 along with the experimental data from Darnton et al.. [12] Following the experimental observations for *E. coli*, we fix the body length at 2.0 μm and flagellar length at 7.5 μm, and choose body widths of either 0.7 μm or 1.0 μm for both the 60-bead swimmer and the 120-bead swimmer. We impose a torque of 1200 pN·nm [12] on each motor in a liquid with viscosity of $\eta = 0.93 \times 10^{-3}$ Pa·s. We find for all cases that the body wobble angle calculated from our model is about 40~46°, which agrees well with the experimental value of about 46°. With the imposed motor torque of 1200 pN·nm, the time constant $\tau = \eta b^3/T$ is computed to be 7.8×10^{-4} s. Using this time constant, the body and bundle rotation rates and the cell speed from the simulations are all lower than measured experimentally, by a factor of 2-3 for the more refined model. As noted earlier, this might be ascribed in part to uncertainty in the torque generated *E. coli*, which does not seem to be known with accuracy. But, it may also be due to inaccuracy in our bead-spring model, which even in the refined version predicts a value of the proportionality coefficient between the torque on a single flagellum and its resulting linear velocity that is lower (by a factor of two or more) than predicted by resistive force theory for slender helices [26].

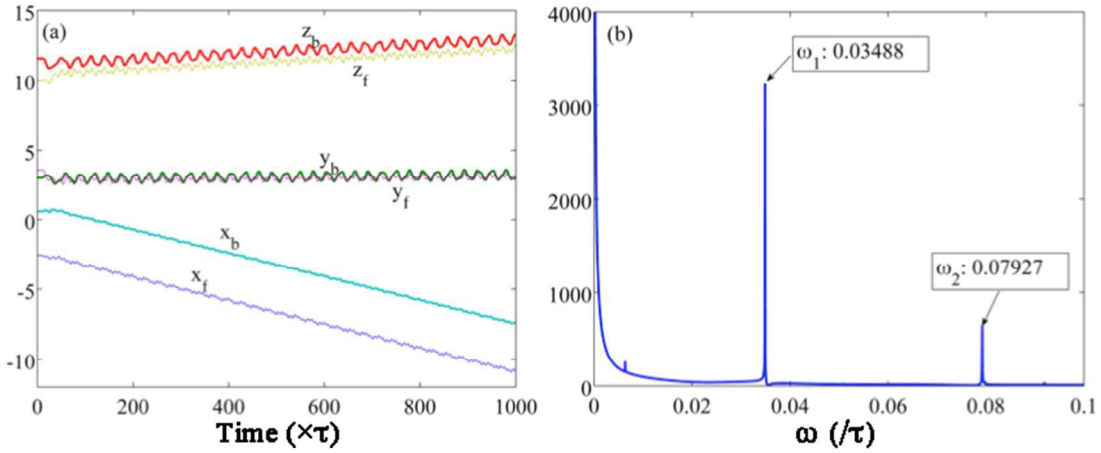

Figure 2 (a) Coordinates (x, y, and z) for a bead on the body (subscript "b") and on a flagellum (subscript "f") for a 60-bead swimmer during running for a period of 1000τ, which is a portion of a run of duration 20000τ; (b) FFT of one of the bead coordinates.

Hereafter, we therefore correct for any inaccuracies in the relationship between motor torque and flagellar rotation speed by limiting our comparisons to ratios of rates. Thus, we compare the ratio of body rotation rate to the bundle rotation rate and the ratio of the cell speed to the bundle rotation rate in Table 1. The coarse-grained (60-bead) swimmer, with body width of 0.7 μm, exhibits a higher ratio of body rotation rate to bundle rotation rate and a lower ratio of the cell speed to the bundle rotation rate than in the experiments. By increasing the body width to 1.0 μm (which remains in agreement with the experimental body width within uncertainties), the ratio of the body rotation rate to the bundle rotation rate is made consistent with the experimental ratio, but the ratio of the cell speed to the bundle ratio becomes much lower than the corresponding experimental ratio. For the refined swimmer (120-bead), the ratio of the body rotation rate to the bundle rotation rate for a body width of 0.7 μm is almost twice the experimental value, while its ratio of cell speed to bundle rotation rate is slightly higher than in the experiments. However, if we increase the body width of the 120-bead swimmer to 1.0 μm to slow down its body rotation rate, we then find that both the ratio of body rotation rate to the bundle rotation rate and the ratio of the cell swimming speed to the bundle rotation rate are reasonably close to the experimental data. This suggests that our detailed 120-bead model with body diameter of 1.0 μm can mimic efficiently the behavior of the *E. coli*, using realistic values of the geometric parameters of *E. coli*. Using this detailed swimmer model, a match of the theoretical flagellar bundle rotation rate, $0.044/\tau$ to the experimental rotation rate 131 Hz, yields a time constant $\tau \approx 0.0003$ s, which sets the "clock" speed for our fine-grained simulations. The time constant for the coarse-grained swimmers determined this way is roughly twice as large as this, $\tau \approx 0.0006$ s. This latter value is close to the value, $\tau = 7.8 \times 10^{-4}$ s estimated using the experimentally estimated torque, T = 1200 pN·nm.

Table 2 Rotation rates, and swimming speeds of the cell during running, compared with experiments

	Experiments [b]	Coarse-grained swimmer (60-bead, three flagella)		Fine-grained swimmer (120-bead, three flagella)	
Body length	2.5±0.6 μm	2.0 b	2.0 b	2.0 b	2.0 b
Body width	0.88±0.09 μm	0.7 b	1.0 b	0.7 b	1.0 b
Bundle length [d]	8.3±2.0 μm	7.5 b	7.5 b	7.5 b	7.5 b
Body wobble angle [c]	46±24 °	43±10 °	46±11 °	40±16 °	40±19 °
Motor rotation rate [e]	154±30 Hz	(0.105±0.008)/ τ	(0.075±0.006)/τ	(0.069±0.001)/τ	(0.054±0.008)/τ
Bundle rotation rate	131±31 Hz	(0.074±0.005)/τ	(0.064±0.005)/τ	(0.049±0.005)/τ	(0.044±0.006)/τ
Body rotation rate	23±8 Hz	(0.031±0.003)/τ	(0.012±0.001)/τ	(0.019±0.003)/τ	(0.010±0.001)/τ
Cell speed	29±6 $\mu m/s$	(0.008±0.001)b/τ	(0.005±0.001)b/τ	(0.013±0.001)b/τ	(0.011±0.002)b/τ
The ratio of bundle to motor rotation rate	0.85	0.70	0.85	0.71	0.81
Ratio of rotation rate of body to bundle	0.18	0.42	0.19	0.39	0.23
Ratio of cell speed to bundle rotation rate (×body width)	0.22	0.15	0.08	0.38	0.25

[a] the values are the means ± standard deviations for both experiments and simulations.

[b] As given in Ref.[12], the experimental data is captured for 32 cells in motility buffer with bulk viscosity 0.93×10^{-3} Pa·s.

[c] The angle swept out by the axis of the cell body as it rolls about the bundle axis.

[d] The distance between the back end of the cell body and the distal end of the bundle.

[e] Since the cell body and the bundle rotate in opposite directions, the motor rotation rate is the sum of the body and bundle rotation rates.

3.2 Tumbling

Figure 3a shows bead coordinates of a typical cell with one of the flagella counter-rotated and changed to semi-coiled, causing it to leave the bundle, and produce tumbling. The thick and thin lines represent beads from the body and the flagellum, respectively. Interestingly, we find that the body has two rotation rates, a normal one, which is similar to that of the body rotation during running, and a much slower one, described by the peak furthest to the left in Figure 3b. The slower of the two rotation rates of the body during tumbling is due to rotation of a long axis of the body around one of the short axes. This occurs as a result of unbundling of a flagellum during tumbling, which miss-aligns the torque of that flagellum away from the direction of the long axis of the body, and requires this long axis to rotate in order to balance the torque on the miss-aligned flagellum. (Movies showing rotation of the long axis are contained in the Supplementary Material.) Using an FFT as described earlier, the rotation rates of the body and flagellum during tumbling are given in Table 3. The rotation rates of the body and flagella are typically somewhat slower (by around 20%) during tumbling than during running.

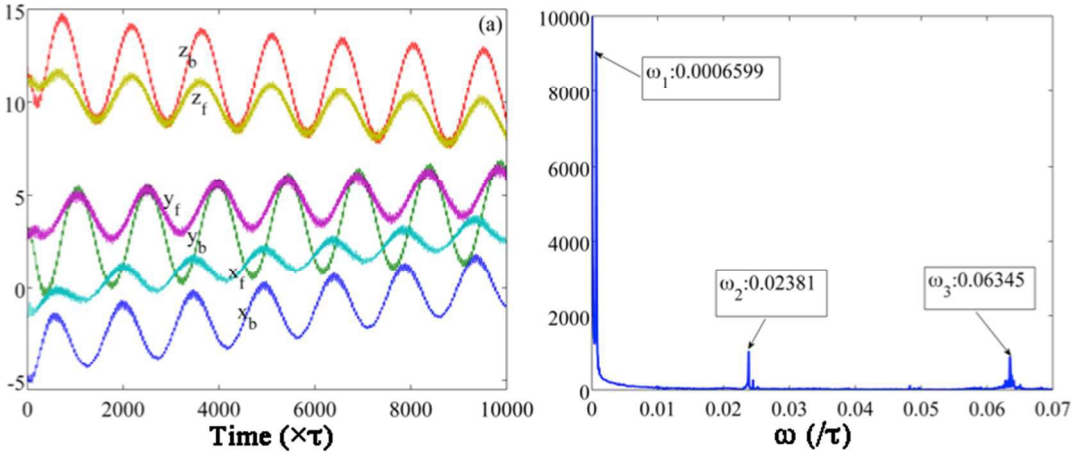

Figure 3 (a) Coordinates (x, y, and z) for a bead on the body (subscript "b") and on a flagellum (subscript "f") for a 60-bead swimmer during tumbling for 10000τ which is part of a tumble of duration 20000τ; (b) FFT of one of the bead coordinates.

Table 3 Rotation speed of body and flagellar bundle during tumbling

	Coarse-grained swimmer (60-bead, three flagellar)		Fine-grained swimmer (120-bead, three flagellar)	
Body length	2.0 *b*	2.0 *b*	2.0 *b*	2.0 *b*
Body width	0.7 *b*	1.0 *b*	0.7 *b*	1.0 *b*
Bundle length	7.5 *b*	7.5 *b*	7.5 *b*	7.5 *b*
Motor rotation rate	(0.086±0.004)/τ	(0.079±0.002)/τ	(0.048±0.002)/τ	(0.040±0.004)/τ
Bundle rotation rate	(0.062±0.002)/τ	(0.064±0.001)/τ	(0.037±0.001)/τ	(0.031±0.004)/τ
Body rotation rate1	(0.0006±0.0001)/τ	(0.0005±0.0001)/τ	(0.0022±0.0007)/τ	(0.0011±0.0003)/τ
Body rotation rate2	(0.024±0.003)/τ	(0.015±0.001)/τ	(0.012±0.001)/τ	(0.008±0.001)/τ
The ratio of bundle to motor rotation rate	0.72	0.81	0.77	0.78
Ratio of body rotation rate1 to bundle rotation rate	0.009	0.008	0.061	0.036
Ratio of body rotation rate2 to bundle rotation rate	0.385	0.232	0.318	0.270

Tumbles are brief events that enable cells to alter swimming direction. A tumbling event begins when one or more flagellar motors change direction of rotation from CCW to CW (as viewed from outside the cell) and ends once all motors have switched back again to CCW. Turner et al. [10] reported the tumbling behaviors of *E. coli* cells with different numbers of flagella undergoing polymorphic transformations from one shape to another, and we wish to compare their observations with the tumbling motions predicted by our whole-swimmer model. Turner et al. reported the total tumbling time to be 0.14±0.08 s, where the 0.08 variability is the standard deviation of many measurements. [10] We choose coarse-grained versions of our *E. coli* model with one tail, two tails, or three tails attached to the middle plane of the body with one tail reversing direction to induce tumbling. Polymorphic transformations of the tail configurations were simulated after 300τ of running with all flagella in their normal helical conformation, followed by 50τ of counter-rotation in the semi-coiled configuration, followed finally by 50τ in the curly 1 configuration. We averaged each result over 50 tumbling motions. The changes in swimming angle during a tumble, which are measured as the difference in angle from the end of one run to the beginning of the next run, for different numbers of flagella, are given in Table 4, where each result is an average value over 50 tumbles. In Table 4, the tumbles lasted for a time of 100τ, which corresponds to around 0.12 s for the coarse-grained swimmer and about half of this value for the fine-grained swimmer, using the bundle rotation speed as the "clock" for measuring time, as described earlier. We find that when the cell has only one filament, the change in direction is about 12-14° for the coarse-grained model and is around 17-25° for the fine-grained model.

Table 4 Tumbling angles of swimmers with different numbers of flagella, for tumbles of duration 200τ with the counter-rotating flagellum in the semi-coiled state during the first half of the tumble and in the curly 1 state during the second half. (The "errors" in this and subsequent tables are standard deviations computed for 50 tumbling events.)

Swimmer	Tumbling Angle (°)					
	Coarse-grained model 15-bead body, 15-bead flagellum			Fine-grained model 30-bead body, 30-bead flagellum		
Number of flagella on a cell	1	2	3	1	2	3
Body width 0.7 *b*	12±6	56±8	58±10	17±7	30±5	29±10
Body width 1.0 *b*	14±4	62±9	48±4	25±6	57±1	45±8

As shown in Figure 4, the onset of a tumble is evident when the bundle loosens near the cell body. Soon thereafter, one flagellum escapes from the bundle, and the cell body changes swimming direction. These filaments undergoing counter-rotation exhibit right-handed waveforms (usually semi-coiled first, and then curly 1), while the motors driving them have switched from CCW to CW. The end of a tumble can be defined experimentally by the establishment of a new well-defined swimming direction or when the filaments return to the bundle, i.e., when the bundle is consolidated. Cells tend to move in a new well-defined direction before consolidation is complete. The sequence of images in Figure 4 is remarkably similar to that seen in experimental images of *E. coli*, in particular Figure 10 in Turner et al. [10], including the total time span encompassed by the image sequence, which is 1/3 s in Turner et al., and is 375τ for the simulations, which corresponds to around 0.22 s.

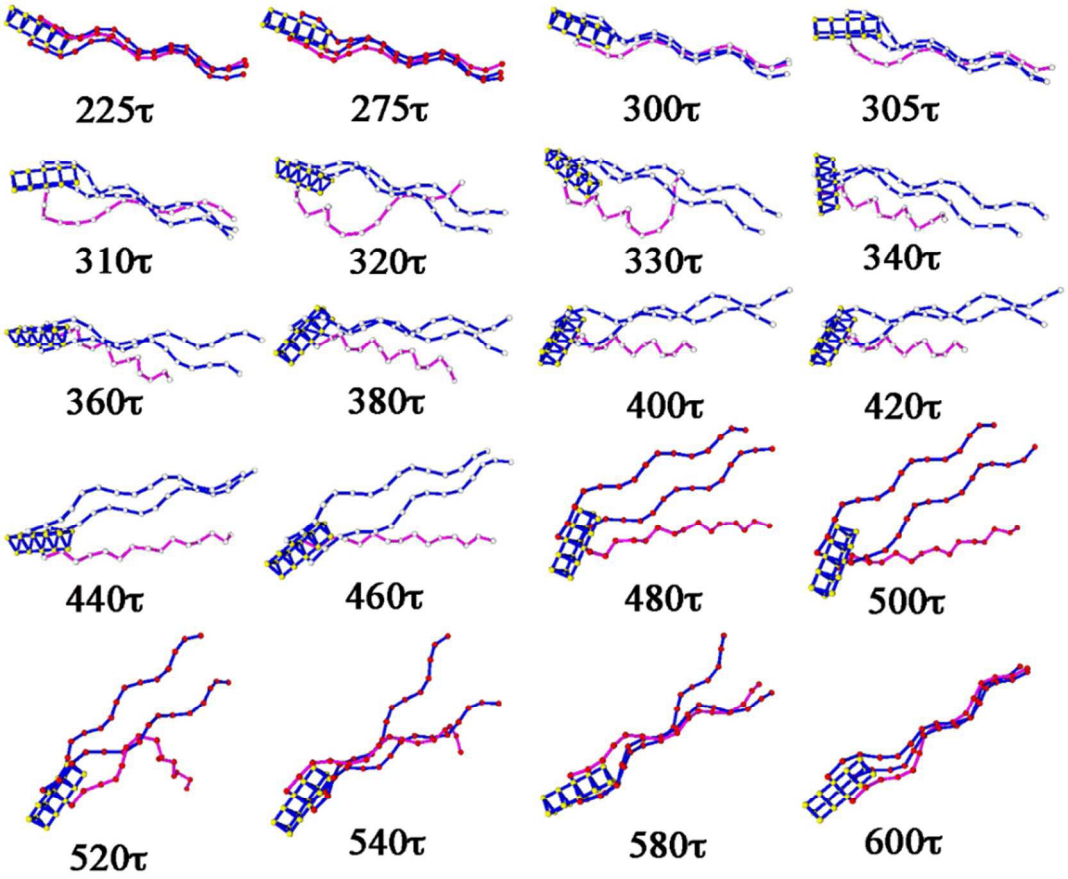

Figure 4 Tumbling of a coarse-grained, thin-body, model *E. coli* with three flagella, one undergoing a polymorphic transformation. The counter-rotation of the unbundling flagellum began at 300τ and ended at 500τ. The normal flagellar shape was semi-coiled between 300τ and 400τ, and was curly 1 between 400τ and 500τ. This figure should be compared to Fig. 10 in Turner et al. [10].

We also consider three different tail arrangements, as shown in Figure 5. In type 1, all three flagella are in the same central plane of the body. In type 2, one flagellum is out of this plane, and in Type 3, all three flagella are in different planes. Various choices were made for the tail chosen to be the one that reverses rotation to produce tumbling. The influence of flagellar attachment locations on average tumbling angles during tumbling is shown in Table 5. For the results in Table 5, the tumbling time is 200τ (corresponding to around 0.06 s for the fine-grained swimmers and 0.12 s for the coarse-grained ones), with the counter-rotating flagellum taking a semi-coiled shape for the first 100τ and a curly 1 shape for the second 100τ. Note that the average tumbling angle changes for different arrangements of flagella on the body, but that they are in reasonable agreement the experimentally determined average value of around 58±40°. [10]

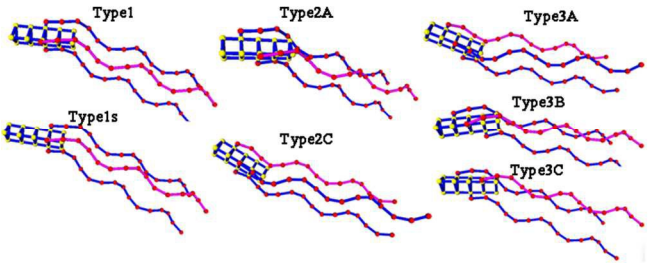

Figure 5 Various three-tail configurations chosen for simulations. For type 1, the three flagella are in the same plane. In type 2, two tails are in the same plane, while the third (tail C) is in the plane closer to the "front" of its body, where the "front" points in the swimming direction. In Type 3, the three tails are in three different planes (called tail A, B, C, ordered starting from the forward end of the body). The flagellum that counter-rotates during tumbling is marked in red.

Table 5 Tumbling angles for swimmers with different arrangements of three flagella on the body, with tumbling time 200τ.

	Tumbling Angle (°)			
	Coarse-grained model 60-bead		Fine-grained model 120-bead	
Body width	0.7 *b*	1.0 *b*	0.7 *b*	1.0 *b*
Type 1	58±10	48±4	27±8	45±8
Type 1s	48±14	36±3	37±6	37±9
Type 2A	47±8	36±5	34±12	38±10
Type 2C	55±3	39±13	17±6	38±9
Type 3A	43±7	35±14	18±6	16±7
Type 3B	42±9	27±7	29±6	32±13
Type 3C	42±8	35±9	46±11	39±11

Next we consider a coarse-grained model for the flagella combined with a refined model for the body, as shown in Table 6, to investigate in more detail how the arrangements of the flagella from the front to the back of the body affect the tumbling angle. As displayed in Table 6, when the swimmer tumbles for a time 100τ, the average tumbling angle depends on the location of attachment of flagella to the body. When the flagella are attached in the middle plane of the body (the fifth layer), we obtain the largest tumbling angle of around 38°. The tumbling angle decreases when the flagella are attached near the front or rear of the body. However, when the tumbling time is increased to 200τ, the tumbling angle is almost independent of layer of attachment. To investigate further dependence of tumbling angle on tumbling time for different arrangements of flagella on the body, we varied the tumbling time from 50τ to 400τ for the flagella with different shapes (normal, semi-coiled and curly1), attached at the middle plane of the body (5th layer), and on the end of the body (8th layer). As shown in Figure 6, for tumbling times of 50τ, 100τ and 150τ, the tumbling angles for flagella attached to the eighth layer of the body are lower than for flagella attached to the middle of the body and increase very roughly linearly with tumbling time. However, for tumbling times of 200τ or larger, the tumbling angles are less sensitive to the arrangement on the body and increase more slowly with tumbling time.

Table 6 Tumbling angles for swimmers with different arrangements of flagella on the body.

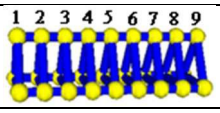	Coarse-grained flagella with 9-layer body (27-bead body and 15-bead flagellum, three flagella) Body length: 2.0 *b*, Body width: 0.7 *b*, Bundle length: 7.5 *b*						
Attachment layer of flagella	2nd layer	3rd layer	4th layer	5th layer	6th layer	7th layer	8th layer
Tumbling angle of 100τ	18±9	22±10	34±6	38±8	32±7	29±5	19±2
Tumbling angle of 200τ	50±9	51±9	50±9	51±6	44±2	51±8	51±10

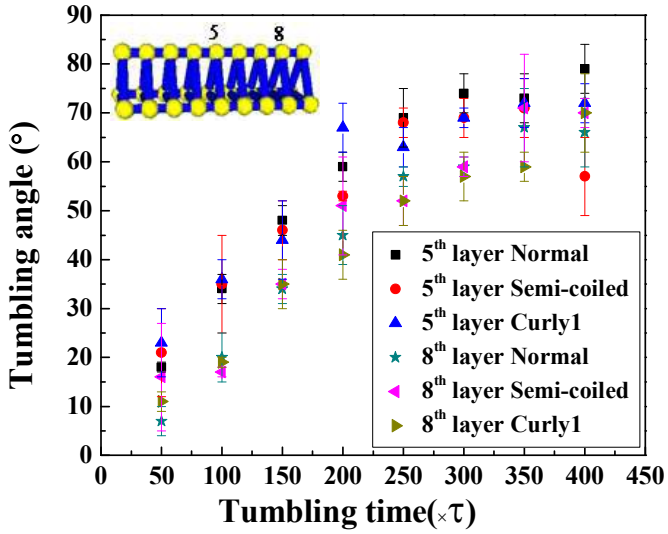

Figure 6 Tumbling angle as a function of tumbling time for different arrangements of flagella on the body and different flagellar shapes during tumbling. Flagella attached on the 5th and 8th layer of the body, respectively, as shown in the inset. Coarse-grained flagella with 9-layer body (27-bead body and 15-bead flagellum, three flagella), body length of 2.0 *b*, body width of 0.7 *b* and Bundle length of 7.5 *b*. Error bars represent standard deviations over 50 repeat runs.

Finally, we note that tumbling can induce an inversion of polarity of the body when flagella are initially attached near the rear of the body, as shown in Table 7. In these simulations, a sequence of runs separated by tumbles is carried out. Depending on the duration of the tumble, the long axis of the body may flip an even or an odd multiple of 180°, resulting in an inversion of the flagellar location, in the case of an odd number of 180° flips.

The simulation tumbling results presented in Tables 4-7 and Figure 6 indicate that the tumbling angle varies widely, from around 10° to around 80°, depending somewhat on flagellar number and arrangement, but especially on tumbling time. The experimental tumbling angle averages around 58°, but is also highly variable, ranging from almost 0° to over 90°. [10] Given that the experimental tumbling time is 0.14 s, with a standard deviation of 0.08 s, in a sample of around 30 or so tumbling events, the tumbling time varies from nearly 0, to over 0.25 s, corresponding roughly to the range of simulated tumbling times reported in Figure 6 and Table 7. Note that the tumbling angles shown over this range are in reasonable agreement with the experimental range, and the mean tumbling angle, corresponding to a tumbling time around 0.14 s or so, is around 50°, in agreement with experimental results.

Table 7 Tumbling motions of swimmer with three flagella initially near the rear of the body as function of tumbling time for a sequence of three run-tumble cycles

Coarse-grained swimmer Three flagella attached on the 8th layer of the body, 27-bead body and 15-bead flagellum Body length: 2.0 b, Body width: 0.7 b, Bundle length: 7.5 b								
Tumbling time	Tumbling angle	Tumbling motions						
33 τ	11±3	Head run	Tumbling	Tail run	Tumbling	Head run	Tumbling	Tail run
67 τ	17±1	Head run	Tumbling	Head run	Tumbling	Head run	Tumbling	Head run
100 τ	28±2	Head run	Tumbling	Tail run	Tumbling	Head run	Tumbling	Tail run
133 τ	31±3	Head run	Tumbling	Head run	Tumbling	Head run	Tumbling	Head run
167 τ	51±9	Head run	Tumbling	Tail run	Tumbling	Head run	Tumbling	Tail run
200 τ	52±5	Head run	Tumbling	Head run	Tumbling	Head run	Tumbling	Head run
220 τ	62±7	Head run	Tumbling	Tail run	Tumbling	Head run	Tumbling	Tail run
275 τ	69±8	Head run	Tumbling	Head run	Tumbling	Head run	Tumbling	Head run
300 τ	70±9	Head run	Tumbling	Tail run	Tumbling	Head run	Tumbling	Tail run
333τ	65±3	Head run	Tumbling	Head run	Tumbling	Head run	Tumbling	Head run
367τ	78±9	Head run	Tumbling	Tail run	Tumbling	Head run	Tumbling	Tail run
390 τ	78±8	Head run	Tumbling	Head run	Tumbling	Head run	Tumbling	Head run

3.3 Additional simulations of bacteria with one flagellum

To investigate why a cell has multiple flagella, we studied the running motions of swimmers with only one flagellum. The following cases were carried out: (1) The rotation of the flagellum was reversed without changing its chirality. In this case, the bacterium swims backwards when the flagellum rotation direction is reversed. (2) Both the rotation direction and the chirality of the flagellum are reversed. In this case, the swimmer simply continues swimming forward. (3) The rotation direction and the handedness of the flagellum are reversed, and flagellar shapes are changed to semi-coiled and to curly 1. In this case, the bacterium tumbles, with tumbling angles given in Table 4. It can be seen that a change of flagellar waveforms is required for the tumbling of the bacterium having only a single flagellum. But the tumbling angle of a swimmer with only one flagellum is small, as shown in Table 4. With increasing numbers of flagella, the tumbling angle increases. This validates the hypothesis by Darnton et al. [12] that multiple, distributed flagella, allows bacteria to change directions more efficiently when they tumble.

4. Conclusions and Future Directions

To study the swimming of the multi-flagellated bacterium Escherichia coli, we deployed a bead-spring model that includes spring, bending and torsional potentials to impose geometrically realistic helical shapes to both the bacterium body and to each of several helical flagella, whose pitch and radius are set by potentials that are adjusted to match the experimental values observed during both running and tumbling of the bacterium. We attached each flagellum to the body at a free hinge, to represent the flexible hook. A torque on the flagellum and counter-torque on the body were imposed using force couples, to mimic the torque generated by the flagellar motor. Hydrodynamic interactions, which create swimming, flagellar bundling, and unbundling during swimming and tumbling, were imposed by treating the beads as Stokeslets, using the Rotne-Prager tensor. Flagella were prevented from passing through each other through short-range repulsions between springs. We explored the behavior of coarse-grained (60-bead) and refined (120-bead) versions of the model, and showed that predictions of running speed, helical and body rotation rates, body wobble rates and angles, average tumbling angles and range of tumbling angles, and flagellar re-bundling times are in reasonable agreement with experimental observations by Berg and coworkers especially for the fine-

grained model. This model, or simplified versions of it, might be used in the future to study the collective behavior of multiple *E. coli* swimmers, or might be modified appropriately to explore other flagellated bacterial swimmers and compare their swimming and tumbling efficiencies with that of *E. coli*.

Acknowledgements

R.G.L. acknowledges the support of the National Science Foundation under grant DMR 1403335. Any opinions, findings, and conclusions or recommendations expressed in this material are those of authors and do not necessarily reflect the views of the National Science Foundation (NSF). M.K. and G.L. acknowledge the financial support from the National Natural Science Foundation of China (51121001).We are grateful for advice of Nobuhiko Watari for the use of the hydrodynamic model of *E. coli* that he developed.

Notes and references

[a] School of aeronautics & astronautics, Sichuan University, Chengdu 610065, PRC
[b] College of polymer science and engineering, State key laboratory of polymer materials engineering of China, Sichuan University, Chengdu 610065, PRC
[c] Department of chemical engineering, University of Michigan, Ann Arbor, Michigan 48109, USA
[d] Department of chemical engineering and materials science, University of Minnesota, Minneapolis, Minnesota 55455, USA

Email:rlarson@umich.edu

1 L. A. Pratt and R. Kolter, *Molecular microbiology*, 1998, **30**, 285-293.
2 L. Hall-Stoodley, J. W. Costerton and P. Stoodley, *Nature Reviews Microbiology*, 2004, **2**, 95-108.
3 R. Di Leonardo, L. Angelani, D. Dell'Arciprete, G. Ruocco, V. Iebba, S. Schippa, M. Conte, F. Mecarini, F. De Angelis and E. Di Fabrizio, *Proceedings of the National Academy of Sciences*, 2010, **107**, 9541-9545.
4 L. Angelani, R. Di Leonardo and G. Ruocco, *Physical review letters*, 2009, **102**, 048104.
5 J. Gachelin, G. Miño, H. Berthet, A. Lindner, A. Rousselet and É. Clément, *Physical review letters*, 2013, **110**, 268103.
6 A. Zöttl and H. Stark, *Physical review letters*, 2014, **112**, 118101.
7 M. Molaei, M. Barry, R. Stocker and J. Sheng, *Physical review letters*, 2014, **113**, 068103.
8 I. Jung, K. Guevorkian and J. M. Valles, *Physical review letters*, 2014, **113**, 218101.
9 M. Ravnik and J. M. Yeomans, *Physical review letters*, 2013, **110**, 026001.
10 L. Turner, W. S. Ryu and H. C. Berg, *Journal of Bacteriology*, 2000, **182**, 2793-2801.
11 H. C. Berg, *E. coli in Motion*, Springer, 2004.
12 N. C. Darnton, L. Turner, S. Rojevsky and H. C. Berg, *Journal of bacteriology*, 2007, **189**, 1756-1764.
13 A. P. Berke, L. Turner, H. C. Berg and E. Lauga, *Physical review letters*, 2008, **101**, 038102.
14 P. T. Underhill, J. P. Hernandez-Ortiz and M. D. Graham, *Physical review letters*, 2008, **100**, 248101.
15 J. P. Hernandez-Ortiz, C. G. Stoltz and M. D. Graham, *Physical review letters*, 2005, **95**, 204501.
16 M. Theers and R. G. Winkler, *Soft matter*, 2014, **10**, 5894-5904.
17 A. Najafi and R. Golestanian, *arXiv preprint cond-mat/0402070*, 2004.
18 C. Pooley, G. Alexander and J. Yeomans, *Physical review letters*, 2007, **99**, 228103.
19 S. Y. Reigh, R. G. Winkler and G. Gompper, *Soft Matter*, 2012, **8**, 4363-4372.
20 S. Y. Reigh, R. G. Winkler and G. Gompper, *PloS one*, 2013, **8**, e70868.
21 M. Ramia, D. Tullock and N. Phan-Thien, *Biophysical journal*, 1993, **65**, 755-778.
22 E. Lauga, W. R. DiLuzio, G. M. Whitesides and H. A. Stone, *Biophysical Journal*, 2006, **90**, 400-412.
23 T. Ishikawa, G. Sekiya, Y. Imai and T. Yamaguchi, *Biophysical journal*, 2007, **93**, 2217-2225.
24 S. Chattopadhyay, R. Moldovan, C. Yeung and X. Wu, *Proceedings of the National Academy of Sciences*, 2006, **103**, 13712-13717.
25 H. Flores, E. Lobaton, S. Méndez-Diez, S. Tlupova and R. Cortez, *Bulletin of mathematical biology*, 2005, **67**, 137-168.
26 N. Watari and R. G. Larson, *Biophysical journal*, 2010, **98**, 12-17.
27 S. P. Holleran and R. G. Larson, *Rheologica Acta*, 2008, **47**, 3-17.
28 H. C. Berg, *Biochemistry*, 2003, **72**, 19.
29 J. Rotne and S. Prager, *The Journal of Chemical Physics*, 1969, **50**, 4831.
30 H. Yamakawa, *The Journal of Chemical Physics*, 1970, **53**, 436.
31 M. Manghi, X. Schlagberger and R. R. Netz, *arXiv preprint cond-mat/0602238*, 2006.

